Ocean Sci. Discuss., 9, 315–357, 2012
www.ocean-sci-discuss.net/9/315/2012/
doi:10.5194/osd-9-315-2012

Ocean Science Discussions

Propagation and dissipation of internal tides in the Oslofjord

A. Staalstrøm[1,2], E. Aas[2], and B. Liljebladh[3]

[1]Norwegian Institute of Water Research, Oslo, Norway
[2]University of Oslo, Oslo, Norway
[3]University of Gothenburg, Gothenburg, Sweden

Received: 22 December 2011 – Accepted: 17 January 2012 – Published: 30 January 2012

Correspondence to: A. Staalstrøm (ans@niva.no)

Published by Copernicus Publications on behalf of the European Geosciences Union.

Abstract

Observations of velocity, pressure, temperature and salinity in the inner Oslofjord have been analysed. The data is used to provide new information about energy dissipation and mixing efficiency of internal tides generated by tidal current across the Drøbak Sill. The ratio between the observed amplitude of the internal wave in the pycnocline and the amplitude of the surface elevation is in the range 38 ± 6 at a distance of 1 km inside the sill and 11 ± 2 at 10 km. The energy flux of the internal wave propagating from the Drøbak Sill into the inner fjord is estimated to vary in the range 155–480 kW. This is the same order of magnitude as the estimated baroclinic energy loss (250 kW). Approximately 40–70 % of this energy flux is dissipated within a distance of 7 km from the sill. The mixing efficiency is estimated to 0.09–0.11 based on energy density and group velocity, and 0.22–0.26 based on perturbation pressure and baroclinic velocity. These numbers are larger than earlier estimates. Only a fraction in the range 0.01–0.03 is transferred to work against buoyancy in the first basin within a distance of 7 km from the sill.

1 Introduction

This paper describes how internal tides propagate away from a sill and how the energy is dissipated as the waves travel away from their creation area. The motivation for the investigation is that dissipation of internal waves plays an important role for the vertical mixing in stagnant fjord basins. Gade (1967) showed how the density of the deep basin water in the Oslofjord is slowly reduced due to vertical diffusion between abrupt deep water renewals. Without this reduction there would be no renewals of the deep water.

The first described observation of internal waves in a sill fjord was made by Petterson at Bornö Hydrographical Station in the Gullmar Fjord on the west coast of Sweden (Zeilon, 1913). In recent years internal waves have been thoroughly studied in this fjord where it is found that 77 % of the internal wave energy dissipates near the sill (Arneborg and Liljebladh, 2001a, b; Arneborg et al., 2004), and it is suggested that this

OSD
9, 315–357, 2012

is due to reflection of internal tides at the fjord head (Arneborg and Liljebladh, 2009).

In the Scottish fjord Loch Etive a tracer experiment showed indirectly that dissipation also take place at the sloping bottom in the inner parts of the fjord (Inall, 2009). Many aspects of the propagation of internal waves have been studied in this fjord (Inall and Rippeth, 2002; Inall et al., 2004; Stashchuk et al., 2007). Another well investigated fjord is the Canadian Knight Inlet, British Columbia (Farmer and Smith, 1978, 1979, 1980; Gargett, 1979; Farmer and Armi, 1999; Afanasyev and Peltier, 2001; Armi and Farmer, 2002; Stacey, 2005), where especially dissipation near the sill is studied, but it is also estimated that approximately two thirds of the barotropic energy loss radiates away from the sill as internal waves (Klymak and Gregg, 2004).

Internal waves in the Oslofjord were first reported by Gade (1967), who also studied the vertical diffusion. Wind stress, wind waves and vertical convection will produce mixing in the surface layer, and Kullenberg (1968, 1971) used rhodamine B experiments in the Oslofjord to express the vertical diffusivity of the surface layer as a function of wind velocity, density stratification and vertical current shear. Shear stress caused by bottom currents will have a similar effect on the waters close to the bottom. Both of these mechanisms produce more homogeneous water masses near the vertical boundaries, while the stratification at mid depths is strengthened. Tidal surface waves can provide the energy required for the mixing in the interior of the water mass. Stigebrandt (1976, 1979, 1999) based his studies of internal waves in the inner Oslofjord on sea level observations, moored current meters and hydrographic data, and he suggested that the vertical diffusion in sill fjords might be driven by internal waves, due to the breaking of these waves at sloping bottoms. The mixed waters would flow back to the interior of the fjord as density currents. For the Oslofjord he assumed that tidal currents above the Drøbak Sill produced such waves. Thorpe (2005) lists four ways by which the tidal energy entering a sill fjord may be lost: reflection of energy from the fjord system back to the open sea as a barotropic wave; loss of energy by the work against the bottom shear stress, particularly over the sill; the generation and maintenance of eddies at the sill; and the generation of internal waves that carry energy into the fjord.

OSD
9, 315–357, 2012

Olsen (1983) compared the vertical diffusivities of the Oslofjord and the Norwegian Coastal Current. Internal waves and vertical diffusion in other Norwegian Fjords have been discussed by Sælen (1948), Fjeldstad (1964), Stigebrandt (1980), Stigebrandt and Aure (1989), and Johnsson et al. (2007). Mathematical solutions of the vertical diffusion including the hypsographic form of the bottom topography were presented by Gade and Edwards (1995). For earlier reviews of mixing, vertical diffusion and other physical processes in fjords, see e.g. Freeland et al. (1980), Farmer and Freeland (1983), Gade et al. (1983), and Svendsen (1986). A recent review of fjord physics has been presented by Inall and Gillibrand (2010).

In this study we have focused on internal waves with tidal periods generated at the Drøbak Sill, since these waves propagate further into the fjord, carrying a considerable amount of energy which will be available for vertical mixing far from the creation area.

The paper is outlined as follows: Sect. 2 describes the area of investigation, the field measurements and databases, and in Sect. 3 we look at the propagation of the internal tides, their phase speeds and amplitudes. In Sect. 4 we estimate how much energy these internal waves are transporting, and the connection between dissipation of internal tidal energy and vertical diffusivity is discussed in Sect. 5.

2 Area of investigation, field measurements and data bases

This section describes the area of investigation, the instrumental set-ups during the main recording period in 2009, as well as the environmental conditions during the period. Other data applied in this study and their sources are also discussed.

2.1 The Oslofjord

A typical fjord is often defined in textbooks (e.g. Syvitski et al., 1987) as an estuary modified by glaciers. A deep inner basin with an almost flat bottom is usually present. The Oslofjord on the other hand is part of a geological rift (Larsen, 2008), and this is

OSD
9, 315–357, 2012

evident in the bathymetry. The fjord can be divided into an outer and an inner part, where the latter is the subject of this study. The two parts are separated by the 12 km long Drøbak Sound, with a shallow sill (19.5 m) at its northern end (Fig. 1a). The special characteristic of the Oslofjord compared to a typical fjord is its complicated topography, especially north of the Drøbak Sill (Fig. 1b). The Håøya Island divides the mouth of the inner fjord into two different channels, the eastern and western inlets. An artificial subsurface wall, the Drøbak Jetty, blocks the western inlet. The jetty has a depth of 1–2 m, except for two 6 m deep openings for smaller vessels. The cross-sectional area over the Drøbak Jetty is only about 10 % of the total cross section at the Drøbak Sill (Aas and Endresen, 1999). In this study we focus on the eastern inlet, which has at least two additional sills, with depths of 47 and 62 m.

The inner fjord takes the shape of a horseshoe, and the two fjord basins, the Vestfjord and the Bunnefjord, are divided by the Nesodden Peninsula. Two sills of approximately 55 m depth extending from the northern tip of Nesodden to the mainland on the other side, separate the two basins (Fig. 1c).

The amplitude of the dominant tidal component M_2 increases from 11.3 cm at Helgeroa (59.00° N 9.85° E) to 14.0 cm at Oslo (59.90° N 10.73° E). The phase shift between Oscarsborg (59.68° N 10.60° E) and Oslo in the inner part of the fjord is smaller than the corresponding shift of a free progressive shallow water wave. Thus the tide behaves like a mixture of a standing and a progressive wave. During spring tides the contributions from the harmonic overtides MS_4, M_4 and $2SM_2$ due to shallow water effects can be clearly seen in the tidal graphs. The average elevation of the sea surface inside the Drøbak Sill from ebb tide to flood is 0.3 m, and the corresponding average transport is 310^3 m^3 s^{-1}. The influence of weather on the water level is frequently of the same order of magnitude as the tidal contribution. The estuarine circulation is relatively weak, since the fresh water supply to the inner fjord during the summer season is typically only 1 % of the tidal transport. This implies that although the tide is small, the tidal transports are still significant, which makes the fjord suitable for studies of tidal effects.

OSD
9, 315–357, 2012

2.2 Recordings and data bases

The main data base consists of an extensive series of hydrographic data recorded between 3 August and 4 September 2009 by seven moorings with a total of six acoustic current profilers (three 190 kHz Nortek Continental, one 600 kHz Nortek Aquadopp, one RDI 300 and one RDI 600), 22 CT/CTD sensors (MicroCAT, SAIV, Aanderaa and YSI), and 23 temperature sensors (Tinytag). To determine the energy flux in the internal waves propagating away from the Drøbak sill, three moorings with CTD sensors were deployed close to moorings with acoustic current profilers at locations S0, S2 and S5 (Fig. 1). In addition an acoustic current profiler with a CTD was deployed at the crest of the Drøbak Sill (S1). The deployment and recovery of the instruments were conducted by R/V *Trygve Braarud*, and in general the data acquisition was successful. The wind conditions were relatively calm with mean wind speeds of 3–5 $m\,s^{-1}$ during the 10 first days of the period, followed by three episodes of strong southerly winds with maximum wind speeds of more than 10 $m\,s^{-1}$ on 15–16 August, 20–23 August, and 27 August–2 September, with calm conditions in between (Fig. 2a). The tidal amplitude of the sea level varied between 10 and 25 cm, with a maximum in the middle of the period (Fig. 2b). Sea level and meteorological data have been obtained from the Norwegian Hydrographic Service and the Norwegian Meteorological Institute.

The temporal variation of the pressure recorded by the moored sensors had three contributions: the varying air pressure, the varying level of the sea surface created by tide and winds, and the shifting tilt of the mooring caused by the strong currents in the Drøbak Sound. The influences of varying air pressure and surface level were corrected for by data from the Meteorological Institute and the Hydrographic Service. The remaining pressure deviations from the nominal depth of the sensors were due to the tilts, and typical deviations during inflows was 0.4 m, with spikes of up to 2.4 m. The resulting errors have been corrected for by linear interpolations of the recorded quantities between the true depths.

OSD
9, 315–357, 2012

Some CTD casts were taken close to the moorings during the period (Fig. 3). These were used to check the depths of the various sensors, as well as the accuracy of the depths of the density surfaces estimated by linear interpolation between these moored sensors. It was found that the error of the estimated depth for the density surfaces is less than one metre at depths of strong stratification like the pycnocline (typically 15–25 m depth), while errors of up to 3 m occur below the pycnocline. The method of linear interpolation between the moored sensors leads to a mean errors in the vertical density gradient of 0.08 kg m^{-4}. 80 % of the error estimates are less than 0.1 kg m^{-4}, but 4 % of the estimates are higher than 0.3 kg m^{-4}, which is of the same order of magnitude as the gradient itself. The mean error estimate is used in Sect. 4 to estimate the accuracy of the calculated energy densities.

Figure 4 presents the current conditions at station S0, S1, S2 and S5. At the last station there was no instrument in the surface layer. Two periods are shown, from 7 to 10 August when the sea surface amplitude was about 11 cm and from 16 to 19 August when the sea surface amplitude was 21 cm. Temperature contours for 8.5, 9, 11, 13, 15 and 17 °C are shown by black contour lines at stations S0, S2 and S5. As is also evident from Fig. 4 the density inside the Drøbak Sill is more nearly homogeneous below the thermocline than outside the sill. At S0 the stratification is more influenced by the effects of changing fresh water supply from outside the Drøbak Sound and changing wind conditions. The data sets give us the opportunity to calculate the densities of potential energy from stratification data and kinetic energy from current data, independent of each other.

Hydrographic stations at different locations in the Oslofjord (S2, S3, S4, S5, S6, S7 and S8, Fig. 1a), sampled by NIVA since 1973 as part of a monitoring program, have been used to determine the average vertical diffusivity in the different basins.

OSD
9, 315–357, 2012

3 Propagation of internal tides

In this section the observations described in Sect. 2 are analysed to obtain the phase speeds, frequencies and amplitudes of the internal tides. The phase speed and frequency are important because they characterize the mode and the origin of the internal wave, and the amplitude is a measure of the wave energy.

3.1 Phase speeds

In a simple two-layer model only one internal mode is possible, and the phase speed is

$$c_i = \sqrt{g' \frac{H_1 H_2}{H_1 + H_2}} \tag{1}$$

where $g' = g(\rho_2 - \rho_1)/\rho_2$ is the reduced gravity, ρ_1 and ρ_2 are the densities of the upper and lower layer, respectively, and H_1 and H_2 are the undisturbed thicknesses of the two layers. Table 1 presents typical characteristics of the Oslofjord, and the ranges in the table reflect the uncertainties of the estimates. The values of H_1 and H_2 in Table 1 will depend on the interpretation of the topography, and similarly g' depends on the value chosen for the density stratification. The range of c_i, based on Table 1 and Eq. (1), then becomes 0.8–1.5 m s^{-1}.

If we apply the observed continuous stratification instead of a two-layer model, many vertical modes of internal waves become possible (e.g. Gill, 1982), and the phase velocity for each mode can be calculated from vertical profiles of the Brunt-Väisälä frequency N, constructed from the recordings of density at the moored sensors. The results are sensitive to the choice of water depth, since deeper waters will produce higher phase speeds. In our calculations a depth range of 80–100 m has been used, and the range for the phase speeds of the first and second internal mode becomes $c_1 = 0.9$–1.1 m s^{-1} and $c_2 = 0.4$–0.5 m s^{-1} at station S2.

OSD
9, 315–357, 2012

The phase speeds can also be determined directly from the observed phase shifts Δt between the stations. We start by estimating the depth z_ρ of the density surface ρ by linear interpolation between the depths of the moored sensors. Vertical displacement profiles $\eta(t,\bar{z}_\rho)$ are constructed by subtracting the running mean depth $\bar{z}_\rho$ of this surface over two tidal cycles from z_ρ,

$$\eta(t,\bar{z}_\rho) = z_\rho - \bar{z}_\rho \tag{2}$$

This definition of η ensures that $\bar{\eta} = 0$, and the vertical displacement at 20 m depth is shown in Fig. 5a. The phase speed can be found from parallel time series of η at two different stations in the fjord. By shifting one of the time series an increasing interval Δt in time until the highest correlation between the two series is found, the phase speed c_ρ of the density surface ρ can be determined from Δt and the distance ΔL between the stations:

$$c_\rho = \frac{\Delta L}{\Delta t} \tag{3}$$

We call this the correlation method. The range of the phase speed c_ρ between S2 and S5 found by using η in (Fig. 5a) and Eq. (3) is then 1.2–1.5 m s^{-1}. This agrees well with the range of c_i found by the two-layer model and with c_1 obtained for the continuous stratification. It is noteworthy that c_ρ is more than twice the speed c_2 found for the second internal mode. We interpret the similarity between c_ρ and c_1 as a confirmation of the dominance of the first mode inside the Drøbak Sill. We will see in Sect. 4.2 that the energy carried by the second mode is much less than the energy carried by the first mode, and that the energy of the second mode is dissipated between station S2 and S5.

According to linear theory (Stigebrandt, 1976) the vertical displacement at the sill should be in phase with the depth-averaged current over the sill. The depth-averaged current measured at S1 is therefore used as a reference. From the estimated phase shift between the vertical displacement at S0 shown in Fig. 5a and the barotropic current over the Drøbak Sill, an outward phase speed of $c_\rho = 0.6$ m s^{-1} can be found using

OSD
9, 315–357, 2012

Eq. (3). The phase speeds of the first and second mode calculated from the density profiles in Fig. 3 are $c_1 = 1.2\,\mathrm{m\,s^{-1}}$ and $c_2 = 0.7\,\mathrm{m\,s^{-1}}$. The similarity between c_ρ and c_2 shows that the second mode was dominant outside the Drøbak Sill during the period of investigation.

In order to estimate the energy transport we need to know which way the internal tides propagate. The already found value of c_ρ between S2 and S5 shows that the internal tide moves inwards from the Drøbak Sill. From Fig. 5a it seems that the phases at both S0 and S5 are delayed compared to S2, indicating that the internal tides have originated at the sill. To investigate this further we have compared the depth-average of the orbital currents above and below 15 m and the vertical displacement at station S2 with the orbital speeds and the displacement of the interface in a two-layer model (Fig. 5b), using the mean values from Table 1. Stigebrandt (1976) solved the linearized shallow-water equations with no rotation for the two-layer case, while applying a local boundary condition at the sill that cancelled the barotropic current in the lower layer. The solution contains a vertical displacement η of the surface between the two layers that propagates as an internal wave in both directions away from the sill. The currents of the internal wave in the two layers have a phase difference of 180° relative to each other. The vertical integral of the baroclinic horizontal velocity from bottom to top obtains the value of zero, implying that only the barotropic current contributes to the depth-averaged current speed. During spring tides, when the surface amplitude a_ζ is about 20 cm, there is a good agreement between the measurements and the theoretical two-layer results (Fig. 5b). This indicates that the internal tide propagates as a first mode progressive wave between S2 and S5, where the energy is not reflected but lost inside the sill. It must be remarked that the agreement is less clear when the tidal forcing is weaker.

A progressive internal wave sets up an orbital speed defined as

$$u' = u - \langle u \rangle_H \tag{4}$$

where u is the current speed in the same direction as the internal wave and $\langle u \rangle_H$ is the barotropic part of the current speed. The barotropic speed is calculated as the

OSD
9, 315–357, 2012

depth-average of the recorded current profile. Fig. 6 presents the phase shift of the baroclinic current estimated from the recordings of the acoustic current profilers using Eq. (4) at station S0, S2 and S5 relative to the phase of the barotropic current over the sill at S1. A positive phase lag means that the phase is smaller than the phase of the barotropic wave at S1. The phase shift according to two-layer theory (Stigebrandt, 1976) for a M_2 wave with c_i set to 1.15 m s^{-1} (the middle point of the range in Table 1) is plotted as solid lines in Fig. 6. The observed baroclinic velocity inside the sill above 20 m and below 40 m agrees well with the theoretical baroclinic wave of the two-layer model propagating into the fjord. Yet the phase shift between 20 and 40 m depth is smaller than what we expected at both station S2 and S5 (Fig. 6). It is thus possible that the two-layer model is too simple to reproduce all aspects of the phase shift. It is also possible that the topography north of the Drøbak Sill may play a role at S2 and S5, either by creating additional internal waves or reflecting internal waves generated at the Drøbak Sill. At S0 the two-layer model fails completely to predict the observed phase shifts. A reason for this could be that the energy is transferred from the first mode to higher modes, as the calculated phase speeds at S0 indicate, and that internal waves generated in the outer fjord may dominate the baroclinic current field in the Drøbak Sound.

3.2 Amplitudes

During the recording period of one month the tidal amplitudes of the surface elevation and the internal wave will vary due to the spring-neap effect, and in order to study the instantaneous amplitude we use what can be called the envelope method. Let $h(t)$ be a time series of the vertical elevation of a surface. Further, let h_1 and h_{99} be the 1 and 99 percentiles of the time series over the running tidal period T from $t - T/2$ to $t + T/2$. These two new time series are assumed to represent the upper and lower rims of the envelope of the time series $h(t)$. The percentiles are used instead of maximum and minimum values in order to remove spikes. The amplitude a_h of h can then be defined as

OSD
9, 315–357, 2012

$$a_h(t) = \frac{1}{2}(h_{99}(t) - h_1(t)) \quad (5)$$

The amplitudes of the vertical displacement, calculated with the envelope method as a function of depth at station S2 and S5, are plotted in Fig. 7a. The mean value ± the standard deviation of the amplitude between 20 and 55 m depth is 5.7 ± 1.0 m and 1.7 ± 0.4 m at stations S2 and S5 respectively, while the maximum amplitudes (7.4 ± 1.3 m at S2 and 3.5 ± 1.0 at S5) are found around a depth of 40 m at both stations. The amplitude of internal waves at 20 to 30 m depth correlates with the amplitude of the sea level elevation. This is not the case deeper down in the water column, and at 40 m depth there is no apparent correlation between amplitudes of the internal wave and the sea surface (Fig. 7b). But there is a correlation at 40 m (not shown here) of 0.62 between the amplitude of the vertical displacement and $|\partial\rho/\partial z|$ at station S2, indicating that greater amplitudes appear when the stratification is stronger at this depth. There is no such correlation at 20 m depth. It is worth noting from Fig. 4 that the amplitudes of the temperature surfaces at station S2 at 40 m depth seem to be greatest in the first period when the amplitude of the sea surface is smallest, and that this can be associated with strong inflows around sill depth.

By applying the definition Eq. (5) to the surface elevation ζ and the internal vertical displacement η, we obtain an ensemble of data for the respective amplitudes a_ζ and a_η that can be used to estimate the amplitude ratio γ defined as

$$\gamma = \frac{a_\eta}{a_\zeta} \quad (6)$$

We will now focus on a_η around the pycnocline since this layer has the strongest correlation to the surface tides (Fig. 7b), and because this layer is also the most energetic as more energy is needed to displace water parcels in strong stratification. Figure 8 presents the amplitudes of the 1023 kg m^{-3} density surface at station S2 and S5 plotted as a function of the sea surface amplitude, obtained from the observed densities by using the envelope method Eq. (5). Estimates of the ratio γ Eq. (6) between the

OSD
9, 315–357, 2012

amplitudes of the interface and the sea surface, based on these measurements, vary in the range 38.4 ± 5.5 at station S2 where the correlation coefficient is 0.69, and in the range 11.2 ± 1.6 at station S5 where the coefficient is 0.80. This means that the amplitude at station S5 is reduced to 20–40 % of the same amplitude at station S2.

In the two-layer solution by Stigebrandt (1976) the phase of the internal wave relative to the sill is a function of the distance x from the sill, expressed by kx, where $k = \omega/c_i$ is the horizontal wave number, and ω is the angular frequency of the semidiurnal tide. The ratio (6), based on Stigebrandt's solution, becomes

$$\gamma = \frac{\omega Y}{A^*} \frac{H_2}{c_i} \tag{7}$$

Here Y denotes the surface area of the fjord inside the sill, and A^* is the cross-sectional area of the channel just outside the sill. The ratio γ has a constant part $H_2 Y/A^*$ depending on the fjord geometry and a varying part ω/c_i depending on the driving force and the stratification. Equation (7) is very useful because it predicts how much energy is likely to be present in the form of internal tides in a sill fjord, prior to any local measurements of surface and internal amplitudes. The insertion of values from Table 1 in Eq. (7) results in estimates of γ in the range 31 ± 15. This compares well with the range for γ found at S2 from Eq. (6). The damping of the vertical displacement further into the fjord, as observed at station S5, was explained by Stigebrandt (1979) as a result of the widening of the fjord. But as we will see in Sect. 5 this effect does not explain all of the damping, and some of the energy must be dissipated between S2 and S5.

3.3 Tidal frequencies

The temporal resolution of 5 and 10 min reveals that there are large vertical movements in the upper 40 m during a tidal cycle (Fig. 4). The frequency spectrum obtained by the Fast Fourier Transform for the 1023 kg m^{-3} density surface at station S2 at around 20 m depth (Fig. 9) exhibits energy peaks near the semidiurnal frequency M_2, as well as at the associated harmonic overtides M_4, M_6 and M_8. For simplicity Fig. 9 attributes all

OSD
9, 315–357, 2012

of the tidal energy to these lunar constituents. The figure displays the same peaks at station S5, but not as clearly. At station S0 outside the sill these peaks are even less significant.

The damping observed at S0 of the internal tides propagating out of the fjord cannot be explained by a widening of the fjord since this part of the fjord south of the sill is almost straight. The most striking difference between the fjord outside and inside the Drøbak Sill is the stronger stratification below sill depth at the outside. It is possible that this contributes to a stronger dampening of the wave in the lower layer.

Examination of echo sounder images from a station in the Bunnefjord close to S8 during the winter of 2009/2010 reveals no signs of first mode internal waves with semidiurnal frequency, even though oscillations with longer and irregular periods are found. (Details of the applied method of analysis have been presented by Kaartvedt et al., 2009).

4 Energy density and energy transport in internal tides

In this section we will use the phase speeds and amplitudes found in the preceding section to calculate the energy density of the internal tides and the corresponding energy flux.

4.1 Calculation of energy density

The energy densities induced by internal tides can be found from the vertical density profiles. If $\eta(t,\bar{z}_\rho)$ is the displacement of a fluid element from its equilibrium position $\bar{z}_\rho$, obtained from Eq. (2), the potential energy per volume unit (in $\mathrm{J\,m^{-3}}$) caused by this displacement can be estimated by the expression (e.g. Gill, 1982 or Cottier et al., 2004)

$$E_\rho(t,\bar{z}_\rho) = -\frac{1}{2} g \overline{\eta^2} \frac{d\bar{\rho}}{dz} = -\frac{1}{4} g a_\eta^2 \frac{d\bar{\rho}}{dz} \tag{8}$$

OSD
9, 315–357, 2012

The harmonic coefficients presented by the Norwegian Hydrographic Service show that the semidiurnal constituents M_2, S_2 and N_2 will dominate the barotropic tide, but the amplitude of the diurnal O_1 is still about 15 % of M_2 in the Oslofjord, and an averaging period of 25 h has therefore been employed to obtain the undisturbed density profile $\bar{\rho}(z)$. This means that Eq. (8) can be regarded as the potential energy density for the internal tides averaged over the tidal period. In the last term it has been assumed that the wave has a sinusoidal shape.

The kinetic energy density of the internal tide averaged over the tidal period can be written

$$E_k(t,z) = \frac{1}{2}\overline{\rho u'^2} \tag{9}$$

where the orbital speed u' is defined by Eq. (4).

In Stigebrandt's two-layer model (1976) the depth-averaged potential energy density caused by the perturbation of the internal wave, when averaged over a tidal period, is

$$\langle E_p \rangle_H = \frac{1}{2} g \overline{\eta^2} \frac{(\rho_2 - \rho_1)}{H} = \frac{\gamma^2 a_\zeta^2}{4} \frac{g(\rho_2 - \rho_1)}{H} = \frac{\gamma^2 a_\zeta^2 c_i^2 \rho_2}{4 H_1 H_2} \tag{10}$$

$\langle\rangle_H$ is the average over the water depth H and $\overline{()}$ is the average over the tidal period T. We have employed $\bar{\eta} = 0$. The corresponding depth and time-averaged kinetic energy density becomes

$$\langle E_p \rangle_H = \overline{\frac{1}{H}\int_{-H}^{\zeta} \frac{1}{2}\rho u'^2 dz} = \frac{\gamma^2 a_\zeta^2 c_i^2}{4H}\left(\frac{\rho_1}{H_1} + \frac{\rho_2}{H_2}\right) \approx \frac{\gamma^2 a_\zeta^2 c_i^2 \rho_2}{4 H_1 H_2} \tag{11}$$

In the last term of Eq. (11) the approximation $\rho_1/\rho_2 \approx 1$ has been used, resulting in an energy density equal to Eq. (10). By taking the sum of Eqs. (10) and (11) we obtain the same total energy density as used by Stigebrandt. We see from Eqs. (10) and (11) that in the special case of two-layer stratification the ratio between the potential and kinetic energy densities is 1.

OSD
9, 315–357, 2012

Energy densities have been calculated from observed density profiles and current measurements using Eqs. (8) and (9) for the stations S0, S2 and S5, and the results are presented in Fig. 10. At all stations the energy density is highest in the upper layer. E_p has a maximum around the pycnocline. S2 is the most energetic station, with a total energy density more than 5 times higher than at the other stations.

At S0 vertical displacement profiles were constructed from temperature rather than density since there were a satisfactory number of sensors for temperature at this station, but not for conductivity. The values of E_p are very low compared to E_k (Fig. 10a). The average in time of the ratio $\langle E_p \rangle_H / \langle E_k \rangle_H$ is 0.004, with periods where it exceeds 0.01. Thus the total energy density of the internal tides outside the Drøbak Sill cannot in this case be calculated from $E = 2E_k$.

Inside the sill the ratio $\langle E_p \rangle_H / \langle E_k \rangle_H$ is closer to 1. Figure 11a demonstrates that at S2 $\langle E_p \rangle_H$ and $\langle E_k \rangle_H$ are almost of the same value until 15 August, but after that date $\langle E_p \rangle_H$ is higher. The mean value of $\langle E_p \rangle_H / \langle E_k \rangle_H \pm$ the standard deviation for the whole period is 1.6 ± 0.6. At S5 $\langle E_p \rangle_H$ is a little lower most of the time, and $\langle E_p \rangle_H / \langle E_k \rangle_H = 0.7 \pm 0.2$.

The errors in the estimates of the density gradients ($0.08\,\mathrm{kg\,m^{-4}}$) and the depth of the density surfaces (1 m) mentioned in Sect. 2 imply that the errors of the calculated potential energy densities are up to 50 %. If the error of the current measurement is $1\,\mathrm{cm\,s^{-1}}$ for a typical current speed of $20\,\mathrm{cm\,s^{-1}}$, the error of the calculated kinetic energy density is only 10 %, but a more serious source of error is the possibility that the baroclinic current calculated from Eqs. (4) may have other causes than just the internal tides. E_k has high values near the surface at station S0 and S2 at approximately the same times as when high wind speeds are observed (Fig. 2a). At S5 there are no current measurements near the surface. The results in Fig. 10 must then be interpreted with caution, but it seems that during the four weeks in 2009 the values of E_p and E_k at S2 and S5 were of the same order of magnitude, while the conditions at S0 were far more difficult to interpret (Fig. 10a and b).

OSD
9, 315–357, 2012

4.2 Estimated energy fluxes

The energy flux associated with internal waves through a cross section A can be written (in units of W)

$$F_i^p = A\left\langle \overline{p'u'} \right\rangle_A \tag{12}$$

where u' is the orbital speed and p' is the perturbation pressure caused by the internal waves. The subscript (i) indicates the station index and the superscript (p in this case) the method. This method is used by for instance Kunze et al. (2002) where the pressure anomaly induced by the internal tide p' is calculated assuming hydrostatic pressure

$$p'(z) = \int_z^0 g\rho'(z')dz' - \left\langle \int_z^0 g\rho'(z')dz' \right\rangle_H \tag{13}$$

and the perturbation density is calculated from

$$\rho' \approx \eta \frac{d\bar{\rho}}{dz} \tag{14}$$

It follows from Gill and Clarke (1974) that $\langle p' \rangle_H = 0$ and this determines the integration constant (second term on the right hand side of Eq. 13). Gill and Clarke assumed a flat bottom in order to separate the horizontal and vertical dependency of the variables. The flat bottom is clearly not the case in the Oslofjord, but compared to the wavelength of the internal tides the bathymetry might be regarded as bottom roughness on an otherwise flat bottom.

By assuming that u' and p' can be separated into time (U_n, P_n) and depth ($\tilde{u}_n$, $\tilde{p}_n$) dependent parts, measurements of currents and stratification can be fitted to the vertical structure of each internal mode n calculated from the mean stratification (e.g. Gill, 1982). The energy flux can then be obtained from

OSD
9, 315–357, 2012

$$F_i^{\mathrm{m}} = A \sum_{n=1}^{\infty} P_n(t) U_n(t) \tilde{u}_n(z) \tilde{p}_n(z) \tag{15}$$

where the superscript m stands for the normal mode method.

An internal wave with a semidiurnal period will have a wavelength of more than 40 km for a phase speed of 1 m s^{-1}. This type of internal wave can be regarded as a long interfacial wave if it occurs in a layer of strong stratification, and its group velocity c_g is therefore approximately the same as the phase velocity. The amount of energy transported by the internal wave away from its area of origin through a vertical section A across the fjord can then be written

$$F_i^{\mathrm{d}} = A \left\langle c_g \left(E_p + E_k \right) \right\rangle_A \tag{16}$$

where the superscript d designates the energy density method.

The energy densities in Eq. (16) can be calculated from the continuous stratification (8 and 9) or by assuming a two-layer stratification (10 and 11). By inserting the two-layer energy densities into Eq. (16) we get

$$F_i^{\mathrm{two}} = \frac{A \rho_2}{2 H_1 H_2} a_\eta^2 c_g^3 \tag{17}$$

where the superscript two means the two-layer method.

Figure 11b and c present an overview of the energy fluxes at station S2 and S5 obtained by using Eqs. (15)–(17). The perturbation pressure method Eq. (12) is only calculated at station S2 (not shown) and agrees well with the results from Eq. (15). Since energy equipartition ($E_p = E_k$) is expected for a wave propagating like an interfacial wave, Eq. (16) most likely overestimates the energy flux at S2 when E_p is higher than E_k (see Fig. 11a). Therefore an alternative version of the energy density method, F_i^{2d}, is shown in Fig. 11 where the energy density is taken as $2E_k$. The mean values during the whole measurement period are summed up in Table 2. It is not clear why the methods based on energy density gives an energy flux that is 2–3 times higher than

OSD
9, 315–357, 2012

when the more diagnostic methods are used. The explanation could be that Eqs. (12) and (15) allows for periods in time or depth intervals where the energy flux is directed out of the fjord, while Eq. (16) assumes that all the energy density is constantly directed into the fjord. When only the positive fluxes are included using Eq. (12) and compared with the original result, the difference indicates that 5–10 % of the energy might be going in the opposite direction at station S2.

The normal mode method Eq. (15) gives the possibility to separate the energy into different normal modes. At S2 87 % of the energy is in the first mode and 13 % in the second mode, while at S5 nearly 100 % of the energy is in the first mode. This means that all of the higher mode energy flux is dissipated between station S2 and S5.

In Sect. 3 the phase speed of the internal tide between the Drøbak Sill and S0 was estimated to be $0.6\,\mathrm{m\,s^{-1}}$. If the energy flux out of the fjord at S0 is estimated by substituting this phase speed for c_ρ in Eq. (16), the result becomes about 300 kW. This result is comparable with the flux at station S2 as shown by Table 2, but the internal tides outside the sill show no sign of propagating like an interfacial wave, as assumed by Eq. (16). The expression (12) gives an energy flux at S0 that is much lower in value and is directed both into and out of the fjord.

5 Dissipation of internal tide energy and vertical diffusivity

In this section energy fluxes found in Sect. 4 are used to identify areas in the fjord with enhanced dissipation, and the differences in the diffusion coefficient calculated for the different basins are tentatively explained by these results.

5.1 Estimates of dissipation

From the moored observations we have calculated the energy flux at stations S2 and S5. The difference between the energy flux into and out of an area represents the energy dissipation in that area. To simplify the analysis the Oslofjord has been divided

OSD
9, 315–357, 2012

into five basins (Fig. 12). Basin 1, 2 and 3 are connected with relatively deep channels of 80–90 m, but they are narrow and the changes of density with time in the different basins differ, indicating that the basins are so closed that vertical mixing processes dominate over horizontal mixing. The energy fluxes at stations S2 and S5 are indicated in Fig. 12.

We have shown that the internal tide propagate as a progressive wave from S2 to S5, indicating that only a small fraction of the energy is reflected (possibly 5–10 %), and hence that the remaining energy is dissipated within the inner fjord. The total amount of energy flux into the inner fjord will also include flux on the western side of the Håøya Island, F_4. We believe that since the cross-sectional area over the Drøbak Jetty on the west side is only about 10 % of the total cross section at the Drøbak Sill (Aas and Endresen, 1999), the flow here will be more jet-like and produce mixing in a confined area, and not much of the energy will propagate away. There are no observations confirming this and the unknown energy flux in the western inlet represents a major uncertainty in the present study. If we assume that $F_4 \ll F_2$ and that no internal wave energy flux is reflected we can say that 155 to 480 kW is dissipated in the inner fjord. No semidiurnal vertical oscillations are found near station S8 (see end of Sect. 3), and this indicates that the energy flux into Basin 5 is zero, and that the dissipation must take place elsewhere (in Basins 1 to 4). For comparison the total barotropic energy flux into the inner fjord between low and high water is approximately 4000 kW. Not all of this is reflected, and the time shift of approximately 5 min between the pressure sensors at stations S1 and S2 suggests a barotropic energy loss of about 250 kW.

The energy flux out of Basin 3 has to go on either side of the Aspond Island (Fig. 1b). The cross-sectional areas of these passages are of the same order of magnitude, and thus it has been assumed that the energy flux is approximately divided in two parts after S3. If we also assume that the damping of the energy flux between the Aspond Island and S5 is small, we can set up the following relationship

$$F_3 \approx 2F_5 \tag{18}$$

where F_3 and F_5 are the energy fluxes past station S3 and S5, respectively (Fig. 12).

OSD
9, 315–357, 2012

We let the energy flux at station S2 (F_2) represent the energy flux into Basin 1 and the energy flux at station S3 the flux out of it (Fig. 12). If there were no dissipation in Basin 1, the difference between F_2 and F_3 would be zero, and the energy flux at S5 would be half the energy flux at S2. This is not the case, and the widening of the fjord does not explain all of the observed damping. By applying values from Table 2 for F_2 and F_5 and using the relationship (18) we obtain a dissipation of energy flux ($F_2 - F_3$) in the range 115–275 kW by using the methods described by the expressions (12), (15), (16) and (17). The relative dissipation r of the energy flux in Basin 1 is

$$r = \frac{F_2 - F_3}{F_2} \tag{19}$$

The results from Eq. (19) are shown in Fig. 11d for the different methods. Depending on which method is used approximately 40–70 % of the energy flux propagating into the inner fjord is dissipated in the eastern channel within a distance of 7 km from the Drøbak Sill, and this is probably the most dissipative region of the fjord.

It has been found in other fjords that most of the dissipation occurs in the vicinity of the sill. Direct measurements of dissipation rates in the Gullmarfjord where the tidal forcing is weaker than in the Oslofjord, indicated that about 77 % of the dissipation took place above the sloping bottom closest to the sill (Arneborg et al., 2004). In Knight Inlet it is found by direct measurements that one third of the barotropic energy loss is dissipated near the sill (Klymak and Gregg, 2004).

5.2 Vertical diffusivity

We will now see how the estimated dissipation is related to the observed vertical diffusivity.

The decrease of the density in closed basins during stagnant periods is a result of work against buoyancy. This work W_g per time and volume unit can be expressed by

OSD
9, 315–357, 2012

$$W_g = -gK_z \frac{d\rho}{dz} \tag{20}$$

where K_z is the coefficient of vertical diffusion, and ρ is the horizontal average of the density over the whole basin. K_z can be calculated from the expression (Gade, 1970)

$$K_z = -\frac{-\int_{-H}^{z} Y \frac{d\rho}{dt} dz'}{Y \frac{d\rho}{dz}} \tag{21}$$

where the time derivative of ρ must be taken during a stagnant period. $Y(z)$ is the hypsographic curve for the basin. The integrated work against buoyancy $\int_V W_g dV$ in unit kW and the depth-averaged diffusivity $\langle K_z \rangle_H$ in unit $\mathrm{cm^2\,s^{-1}}$ below 20 m is given for each basin in Fig. 12. The results are obtained from observations made during May–September 2003. It is noteworthy that the diffusivity is more than 10 times higher in Basin 1 than in Basin 2, and that the diffusivity in Basin 5 is the lowest one of the five basins. This is consistent with results that have been repeatedly obtained during the monitoring program for the Oslofjord since it started in 1973, and the ratios between the diffusivities in each basin are persistent.

The mixing efficiency R_f of a basin can be expressed by

$$R_\mathrm{f} = \frac{\int_V W_g dV}{\Delta F} \tag{22}$$

where V is the volume of the basin, W_g is defined by Eq. (20) and $\Delta F = F_\mathrm{in} - F_\mathrm{out}$ is the net flux of internal wave energy into the volume. ΔF contains both the kinetic and potential wave energy. Traditionally the symbol R_f is used for the flux Richardson number defined as the ratio between the work against buoyancy and the kinetic energy. Stigebrandt (1976) assumed that all the internal wave energy was converted to turbulent energy below sill depth and termed Eq. (22) the flux Richardson number, but we will not make that assumption here, and we will refer to Eq. (22) as the mixing efficiency.

The sum of the work against buoyancy of the Basins 1–4 is 41 kW. Basin 5 has not been included since the energy flux into this basin is practically zero. This gives an

OSD
9, 315–357, 2012

overall mixing efficiency Eq. (22) in the range 0.09–0.11 (Table 2) if the flux is calculated from methods based on energy density (16 or 17). If the energy flux is obtained from the perturbation pressure (12 or 15), the mixing efficiency R_f increases to 0.22–0.26. Stigebrandt (1976) estimated the same efficiency to be 0.05 by using Eq. (17). Only the spring tide was then considered since his energy flux was a sum of the tidal constituents. In the present study the most efficient mixing is found during neap tides when the energy flux is at its minimum. We believe that during more energetic periods of the spring-neap cycle more of the energy of the internal tides is transferred to processes like e.g. horizontal eddies near the sill than to vertical mixing. We expected that a period with increased energy flux would be followed by a period with increased work against buoyancy. But by looking at the density change in 78 m at S5 (not shown) no signs are found of a direct relationship between the energy dissipation and the change in basin density on shorter timescales (days). We think that this is because the mixing is a result of both local processes and internal waves that release parts of their energy elsewhere in the fjord.

The mixing efficiency in the most energetic basin is low (0.01–0.03), and this agrees with data presented by Stigebrandt and Aure (1989) indicating that more energetic basins have lower mixing efficiencies.

The fate of the 30–60 % of the energy that is not dissipated in Basin 1 is not known, but it seems like this remaining energy is very important for the vertical mixing in the less energetic parts of the inner fjord, since mixing efficiency is expected to be higher for these parts. Bjerkeng et al. (1978) found that the diffusivity calculated from observations of a passive tracer in the middle of the Vestfjord (Basin 3) was one order of magnitude lower than the diffusivity calculated from the budget method, and Stigebrandt (1979) suggested that this was because the diffusivity was higher around the basin borders where the breaking of internal waves is assumed to take place.

OSD
9, 315–357, 2012

6 Summary and final remarks

Observations of vertical displacement in the Oslofjord inside the Drøbak Sill have revealed that there is a linear relationship between the amplitude of the vertical displacement in the pycnocline and the tidal forcing, at both station S2 and S5. This can be explained by a two-layer model, where the interfacial wave sets up a baroclinic current that annihilates the barotropic current in the lower layer at the position of the sill. The ratio between the amplitudes of the internal wave in the pycnocline and the surface elevation is in the range 38 ± 6 at a distance of 1 km inside the Drøbak Sill, 11 ± 2 at 10 km, and 31 ± 15 when estimated from the two-layer model. Great vertical displacements of the density surfaces are observed below the pycnocline, but this seems to be associated with jet-like currents at sill depth and is not a linear response to the tidal currents. When the inflowing current is positioned just above the sill depth, a jet seems to form that depresses the density surfaces below even further down. This process depends on the vertical current profile and is not directly dependent on the tidal forcing. As a result the amplitude of the vertical displacement at for instance 40 m depth at station S2 is not correlated with the amplitude of the sea level elevation.

The observed phase speeds in the range 1.2–1.5 $\mathrm{m\,s^{-1}}$ into the fjord and approximately 0.6 $\mathrm{m\,s^{-1}}$ out of the fjord indicate that the first internal mode dominates inside the Drøbak Sill, while the second mode dominates at the outside. This can probably be explained by the stronger density stratification in the lower layer outside the sill. About 13 % of the energy flux at station S2 is carried by the second internal mode, and all of this energy flux is dissipated between S2 and S5. The much more efficient dissipation of the higher modes might explain why the semidiurnal internal waves at S0 are only found in shorter time intervals when the tides are strong (Fig. 5a) and not for most of the period (Fig. 9).

The energy flux obtained from observed internal tidal energy density and estimated group speed (Eqs. 16 and 17) is 2–3 times higher than the energy flux found from perturbation pressure and baroclinic velocity (Eq. 12) and (Eq. 15) (see Table 2). This can

OSD
9, 315–357, 2012

partly be explained by the fact that methods based on perturbation pressure allow for negative energy flux in some periods of time or in parts of the depth interval. But only 10 % of the energy flux calculated from Eq. (12) at S2 is reflected, so another possibility is that not all of the observed energy density is propagating away from the sill, or that the propagation speed of the energy is lower than the first mode phase speed. Xing and Davis (2011) found in a model study of a sill fjord with a sill depth of 30 m that the baroclinic energy flux was reduced to 20–30 % when a second sill was introduced 1.5 to 2.5 km further into the fjord, and that standing internal tides were generated between the sills. It could be that the relatively high levels of perturbation energy density observed at S2 are due to standing waves. The data base available offers no definite answer as to which method gives the most realistic picture, so we can only conclude that a different choice of method gives different results for the mixing efficiency in the Oslofjord. Mixing efficiency based on energy fluxes calculated from the energy density method gives values for R_f in the range 0.09–0.11, while the perturbation pressure method gives values for R_f in the range 0.22–0.26.

In the most energetic basin (Basin 1) the energy efficiency is the lowest (0.01–0.03). This agrees with earlier results (Stigebrandt and Aure, 1989). Inall et al. (2005) found that as much as 30–40 % of the barotropic energy loss at the sill in Loch Etive was transformed to horizontal eddies and it is known that the area north of the Drøbak Sill also produces horizontal eddies (e.g. Gade, 1963).

Acknowledgements. This project – Tidally-induced turbulent mixing in a silled fjord (Pro. no. 184944) – has been supported by the Norwegian Research Council.

Thanks are due to Jan Magnusson and the crew on board the R/V *Trygve Braarud* for their assistance during the field work, as well as to Göran Broström and Lars Petter Røed for constructive discussions and suggestions.

OSD
9, 315–357, 2012

References

Aas, E. and Endresen, Ø.: Accuracy of simplified transport estimations in narrow sea straits, Ocean Dynam., 51, 441–451, 1999.

Afanasyev, Y. D. and Peltier, W. R.: On breaking internal waves over the sill in Knight Inlet, Proc. R. Soc. Lond. A, 457, 2700–2825, 2001.

Armi, L. and Farmer, D.: Stratified flow over topography: bifurcation fronts and transition to the uncontrolled state, Proc. R. Soc. Lond. A, 458, 513–538, 2002.

Arneborg, L. and Liljebladh, B.: The internal Seiches in Gullmar Fjord, Part I: Dynamics, J. Phys. Oceanogr., 31, 2549–2566, 2001a.

Arneborg, L. and Liljebladh, B.: The internal Seiches in Gullmar Fjord, Part II: Contribution to basin water mixing, J. Phys. Oceanogr., 31, 2567–2574, 2001b.

Arneborg, L. and Liljebladh, B.: Overturning and dissipation caused by baroclinic tidal flow near the sill of a fjord basin, J. Phys. Oceanogr., 39, 2156–2174, 2009.

Arneborg, L., Janzen, C., Liljebladh, B., Rippeth, T. P., Simpson, J., and Stigebrandt, A.: Spatial variability of diapycnal mixing and turbulent dissipation rates in a stagnant fjord basin, J. Phys. Oceanogr., 34, 1679–1691, 2004.

Bjerkeng, B., Göranson, C. G., and Magnusson, J.: Investigations of different alternatives for waste water disposal from Sentralanlegg Vest, NIVA Rep. No. 013276, 74 pp., 1978 (in Norwegian).

Cottier, F., Inall, M., and Griffiths, C.: Seasonal variations in internal wave energy in a Scottish sea loch, Ocean Dynam., 54, 340–347, 2004.

Farmer, D. M. and Armi, L.: Stratified flow over topography: the role of small-scale entrainment and mixing in flow establishment, Proc. R. Soc. Lond. A, 455, 3221–3258, 1999.

Farmer, D. M. and Freeland, H. J.: The physical oceanography of fjords, in: Progress in Oceanography, edited by: Angel, M. V. and O'Brien, J. J., Pergamon Press, Oxford, Vol. 12, 147–219, 1983.

Farmer, D. M. and Smith, J. D.: Nonlinear internal waves in a fjord, in: Hydrodynamics of Estuaries and Fjords, edited by: Nihoul, J., Elsevier, 465–493, 1978.

Farmer, D. M. and Smith, J. D.: Generation of lee waves over the sill in Knight Inlet, in: Fjord Oceanography, edited by: Freeland, H. J., Farmer, D. M., and Levings, C. D., Plenum Press, 259–269, 1979.

Farmer, D. M. and Smith, J. D.: Tidal interaction of stratified flow with a sill in Knight Inlet,

OSD
9, 315–357, 2012

Deep-Sea Res., 27A, 239–254, 1980.
Fjeldstad, J. E.: Internal waves of tidal origin, Geofys. Publ., 25, 73 pp., 1964.
Freeland, H. J., Farmer, D. M., and Levings, C. D. (Eds.): Fjord Oceanography, NATO Conference Series, Plenum Press, New York, Vol. 4, 715 pp., 1980.
Gade, H. G.: Some hydrographic observations of the inner Oslofjord during 1959, Hvalråd. Skr., 46, 62 pp., 1963.
Gade, H. G.: The Oslofjord and its pollution problems, Investigations 1962–1965, Report no. 2, Hydrography (in Norwegian), NIVA report OR-0191c, 163 pp., 1967.
Gade, H. G.: Hydrographic investigations in the Oslofjord, a study of water circulation and exchange processes, Geophys. Inst. Div. A, Rep 24, 1970.
Gade, H. G. and Edwards, A.: Topographic influence on determination of one-dimensional vertical diffusivity in sea basins, Geophys. Inst., Univ. Bergen, Rep. No. 73, 20 pp., 1995.
Gade, H. G., Edwards, A., and Svendsen, H.: Coastal Oceanography, NATO Conference Series, Vol. 11, Plenum Press, New York, 582 pp., 1983.
Gargett, A. E.: Turbulence measurements through a train of breaking internal waves in Knight Inlet, BC, in: Fjord Oceanography, edited by: Freeland, H. J., Farmer, D. M., and Levings, C. D., Plenum Press, 277–281, 1979.
Gill, A. E.: Atmosphere-Ocean Dynamics, Academic press, San Diego, Calif., 662 pp., 1982.
Gill, A. E. and Clarke, A. J.: Wind-induced upwelling, coastal currents and sea-level changes, Deep-Sea Res., 21, 325–345, 1974.
Inall, M. E.: Internal wave induced dispersion and mixing on a sloping boundary, Geophys. Res. Lett., 36, L05604, doi:10.1029/2008GL036849, 2009.
Inall, M. E. and Gillibrand, P. A.: The physics of mid-latitude fjords: a review, Geological Society, London, Special Publications, 344, 17-33, 2010.
Inall, M. E. and Rippeth, T. P.: Dissipation of tidal energy and associated mixing in a wide fjord, Environm. Fluid Mech., 2, 219–240, 2002.
Inall, M. E., Cottier, F. Griffiths, C., and Rippeth, T.: Sill dynamics and energy transformation in a jet fjord, Ocean Dynam., 54, 307–314, doi:10.1007/s10236-003-0059-2, 2004.
Johnsson, M., Green, J. A., and Stigebrandt, A.: Baroclinic wave drag from two closely spaced sills in a narrow fjord as inferred from basin water mixing, J. Geophys. Res., 112, C11002, doi:10.1029/2006JC003694, 2007.
Kaartvedt, S., Røstad, A., and Klevjer, T. A.: Sprat Sprattus sprattus can exploit low oxygen waters for overwintering, Mar. Ecol. Prog. Ser., 390, 237–249, doi:10.3354/meps08196, 2009.

OSD
9, 315–357, 2012

Klymak, J. M. and Gregg, M. C.: Tidally generated turbulence over the Knight Inlet Sill, J. Phys. Oceanogr., 34, 1135–1151, 2004.
Kullenberg, G.: Measurements of horizontal and vertical diffusion in coastal waters, Dept. Phys. Oceanogr., Univ. Copenhagen, Rep. No. 3, 66 pp., 1968.
Kullenberg, G.: Results of diffusion experiments in the upper region of the sea, Dept. Phys. Oceanogr., Univ. Copenhagen, Rep. No. 12, 66 pp., 1971.
Kunze, E., Rosenfeld, L. K., Carter, G. S., and Gregg, M. C.: Internal waves in Monterey submarine canyon, J. Phys. Oceanogr., 32, 1890–1913, 2002.
Larsen, T. L., Olaussen, S., Sundvoll, B., and Heeremans, M.: The Permo-Carboniferous Oslo Rift through six stages and 65 million years, Episodes, 31, 52–58, 2008.
Lepland, Ai., Bøe, R., Lepland, Aa., and Totland, O.: Monitoring the volume and lateral spread of disposed sediments by acoustic methods, Oslo Harbor, Norway, J. Envir. Man., 90, 3589–3598, 2009.
Olsen, R. B.: Vertical diffusion coefficients in the Coastal Current and in the Oslofjord, and the relation to other oceanographic parameters, Thesis, Dept. Geophys., Univ. Oslo, 128 pp., 1983(in Norwegian).
Stacey, M. W.: Review of the partition of tidal energy in five Canadian fjords, J. Coast. Res., 21, 731–746, 2005.
Stashchuk, N., Inall, M., and Vlasenko, V.: Analysis of supercritical stratified tidal flow in a Scottish fjord, J. Phys. Oceanogr., 37, 1793–1810, 2007.
Stigebrandt, A.: Vertical diffusion driven by internal waves in a sill fjord, J. Phys. Oceanogr., 6, 486–495, 1976.
Stigebrandt, A.: Observational evidence for vertical diffusion driven by internal waves of tidal origin in the Oslofjord, J. Phys. Oceanogr., 9, 435–441, 1979.
Stigebrandt, A.: Some aspects of tidal interaction with fjord constrictions, Estuar. Coast. Mar. Sci., 11, 151–166, 1980.
Stigebrandt, A.: Resistance to barotropic tidal flow in straits by baroclinic wave drag, J. Phys. Oceanogr., 29, 191–197, 1999.
Stigebrandt, A. and Aure, J.: Vertical mixing in basin waters of fjords, J. Phys. Oceanogr., 19, 917–926, 1989.
Svendsen, H.: Mixing and exchange processes in estuaries, fjords and shelf waters, in: The Role of Freshwatwer Outflow in Coastal Marine Ecosystems, NATO ASI Series, Vol. G7, edited by: Skreslet, S., Springer-Verlag Berlin Heidelberg, 13–45, 1986.

OSD
9, 315–357, 2012

Syvitski, J. P. M., Burrell, D. C., and Skei, J. M.: Fjords – Processes and Products, Springer-Verlag, New York Inc., 379 pp., 1987.
Sælen, O. H.: Temperature variations and heat transport in the Nordfjord, Bergen Museums årbok 1946–47, Nat. Vit. rekke, 6, 28 pp., 1948.
Thorpe, S. A.: The Turbulent Ocean. Cambridge University Press, 439 pp., 2005.
Xing, J. and Davies A. M.: On the interaction of internal tides over two adjacent sills in a fjord, J. Geophys. Res., 116, doi:10.1029/2010JC006333, 2011.
Zeilon, N.: On the seiches of the Gullmar Fjord, Svenska Hydrog.-Biolog. Komm. Skrifter, 5, 1–17, 1913.

OSD
9, 315–357, 2012

Table 1. Characteristic parameters for the Oslofjord. The ranges are representative minimum and maximum values.

Parameter	Description	Range
A^*	Cross-sectional area of the fjord just outside the Drøbak sill	$(60–70) \times 10^3$ m^2
Y	Horizontal area of the surface inside the Drøbak sill	$(188–192) \times 10^6$ m^2
ω_n	Angular frequency	$(1.40–1.45) \times 10^{-4}$ s^{-1}
H_1	Thickness of the upper layer or sill depth	(15–20) m
H_2	Thickness of the lower layer or height of the sill over the bottom	(60–80) m
Δ_ρ	Difference between the mean densities above and below sill depth	(5–15) kg m^{-3}

OSD
9, 315–357, 2012

Table 2. Mean energy fluxes and mixing efficiency during the measurement period. Mixing efficiency on the east side of Håøya Island (Basin 1) and in the entire western part of the inner Oslofjord (Basins 1 to 4) is calculated by using values for work against buoyancy from Fig. 12.

Method	Energy flux at station S2 (kW)	Energy flux at station S5 (kW)	Energy loss in Basin 1 (kW)	Ratio r (19)	R_f in Basin 1	R_f in Basins 1 to 4
Energy density method F^{d} (16)	480	145	190	40 %	0.02	0.09
Energy density method with energy equipartition F^{2d}.	370	115	140	40 %	0.02	0.11
Two-layer method F^{two} (17)	385	55	275	70 %	0.01	0.11
Normal mode method F^{m} (15)	155	30	95	60 %	0.03	0.26
Perturbation pressure method F^{p} (12)	185					0.22

OSD
9, 315–357, 2012

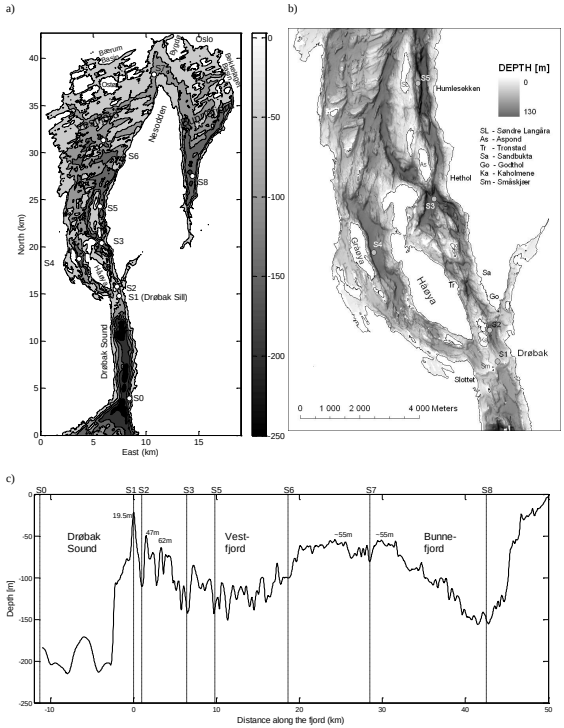

Fig. 1. **(a)** Map of the inner Oslofjord. Depth contours are drawn for every 50 m. Moorings were deployed at station S0 (Brenntangen), S1 (Drøbak Sill), S2 (Kaholmen) and S5 (Søndre Langåra). Station S3, S4, S5, S6, S7 and S8 marked with white circles are standard hydrographic stations from the monitoring program. **(b)** Map of the area around the Drøbak Sill. Bathymetric data are from the Geological Survey of Norway (Lepland et al., 2009). A grey scale indicates the depths down to 130 m. A hillside shade effect is used to emphasize the bathymetric structure. Stations are marked with grey cricles. The subsurface Drøbak Jetty runs from Kaholmen to Småskjær and further to Slottet on the west side of the sound. The Drøbak Sill (19.5 m) is located between Småskjær and Drøbak. There is a sill between Kaholmen and Godthol (47 m) and another one between Tronstad and Sandbukta (62 m). **(c)** Depth profile along the fjord following the deepest parts from the Drøbak Sound, on the east side of Håøya Island to the inner parts of the Bunnefjord. Vertical dashed lines indicate the positions of the stations along this line. The most important sills – the Drøbak Sill (19.5 m), the Godthol Sill (47 m), the Tronstad Sill (62 m) and the two sills between the Vestfjord and the Bunnefjord (55 m) – are marked with numbers.

OSD
9, 315–357, 2012

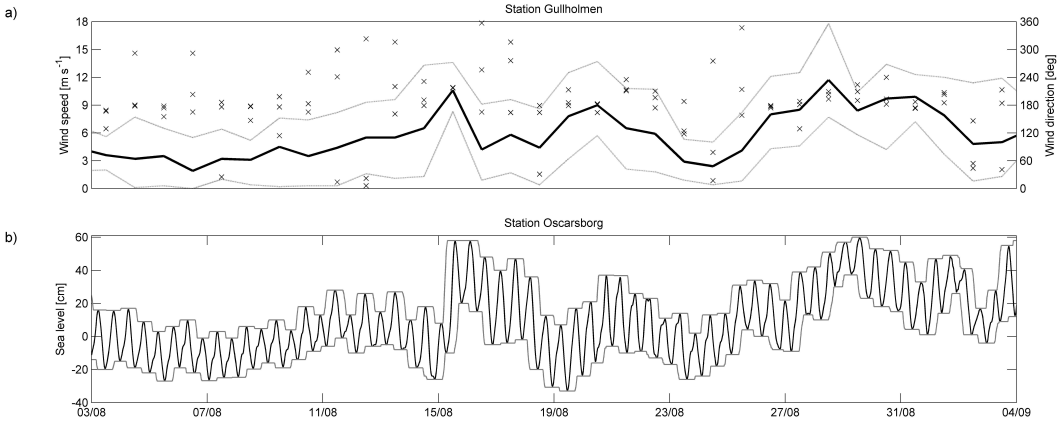

Fig. 2. **(a)** The wind conditions at the station Gullholmen approximately 26 km south of the Drøbak Sill. The thick black line represents the diurnal mean wind speed, the dotted lines the diurnal maxima and minima of the speed, and the crosses mark the wind directions. **(b)** Sea level measured at the station Oscarsborg close to S2 (black line). Grey lines indicate the 1 and 99 percentile levels of the sea level during a tidal cycle. These levels are used in Eq. (5) to calculate the amplitude of the sea level.

OSD
9, 315–357, 2012

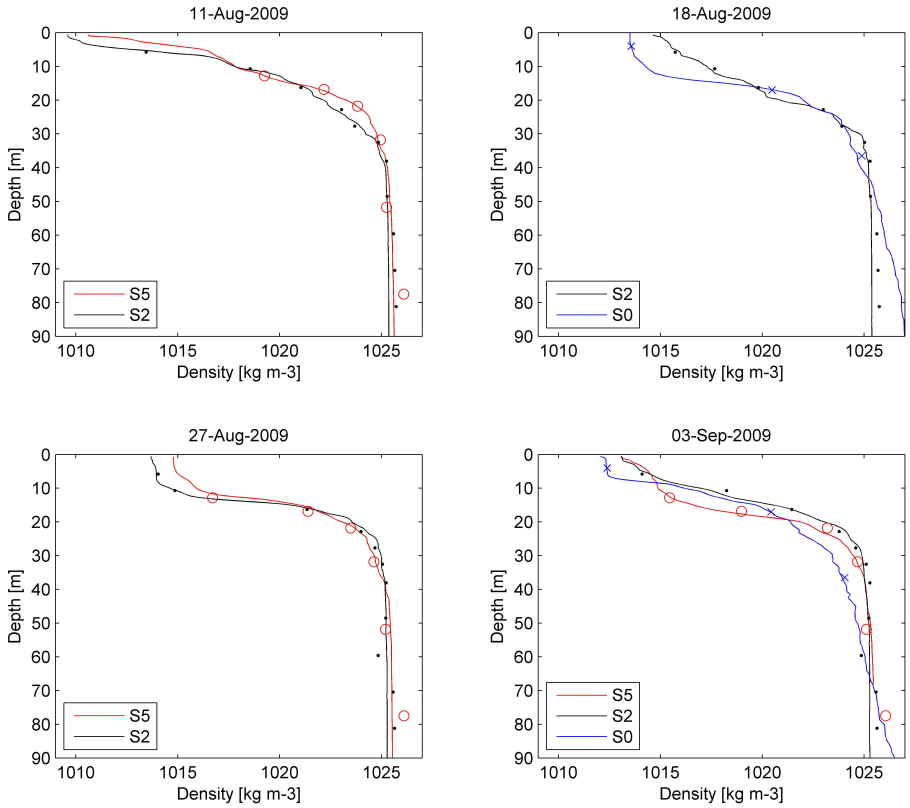

Fig. 3. Comparison between density profiles measured with a CTD (lines) and moored instruments (symbols) at four different dates.

OSD
9, 315–357, 2012

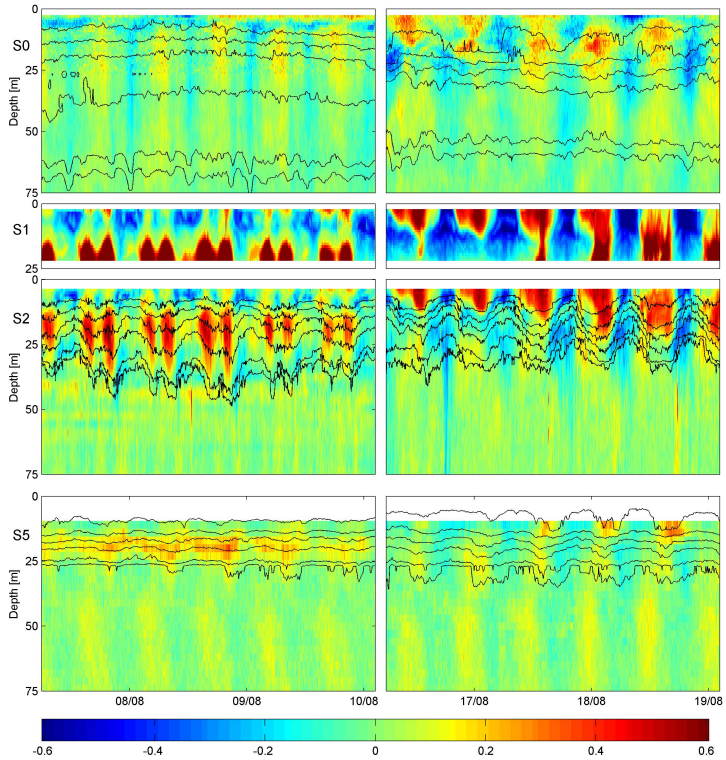

Fig. 4. The current speed along the fjord measured with acoustic current profilers at station S0 (Brenntangen), S1 (Drøbak sill), S2 (Kaholmen) and S5 (Søndre Langåra) is shown with a colourscale where red indicates current into and blue current out of the fjord. Temperatures of 8.5, 9, 11, 13, 15 and 17 °C increasing upwards are shown by black contour lines at stations S0, S2 and S5. The temperature has been interpolated linearly between the depths of the moored instruments. Two periods are shown, from 7 to 10 August when the sea surface amplitude was about 11 cm and from 16 to 19 August when the amplitude was 21 cm.

OSD
9, 315–357, 2012

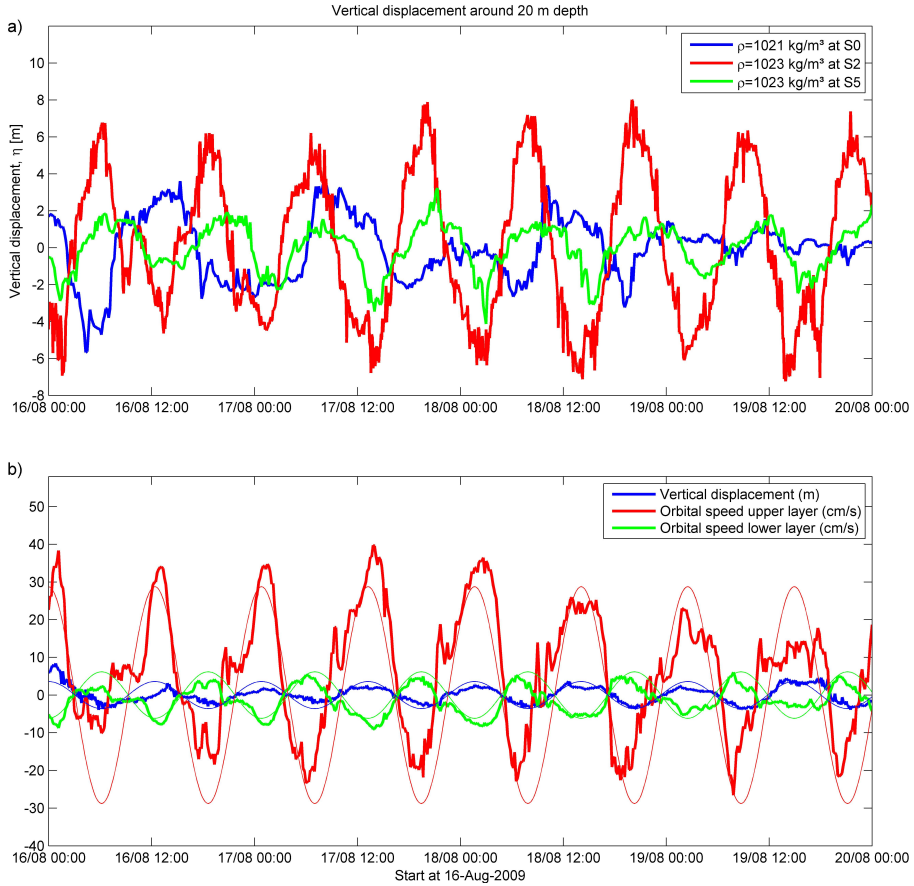

Fig. 5. **(a)** Vertical displacement of density surfaces at station S0, S2 and S5 at 20 m depth. **(b)** Vertical displacement and orbital speed in the upper and lower layer at station S2, bold lines are the results from measurements and thin lines are results from a two-layer model.

OSD
9, 315–357, 2012

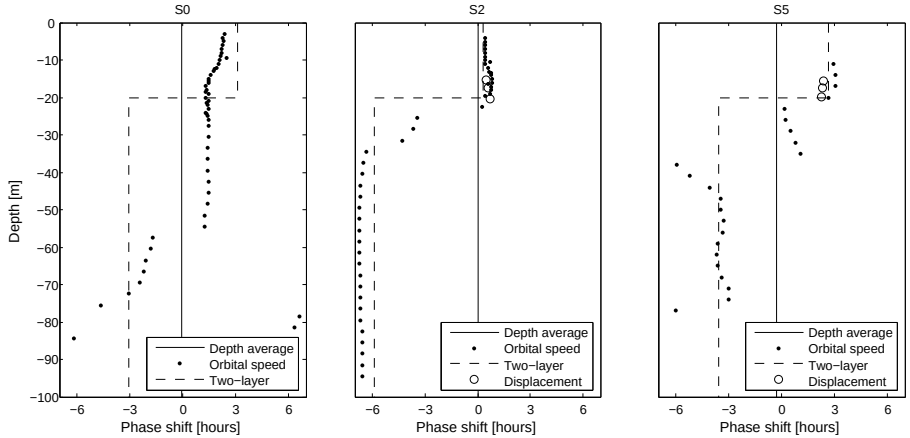

Fig. 6. Phase shift of the current measurements at station S0 (left), S2 (middle) and S5 (right) relative to the depth-averaged current over the Drøbak Sill (station S1). The vertical solid line is the phase (= 0) of the depth-averaged current. The black dots are the phase shifts of the measured baroclinic current Eq. (4) as a function of depth, and the dashed lines are the theoretical phase shifts from two-layer theory and Table 1.

OSD
9, 315–357, 2012

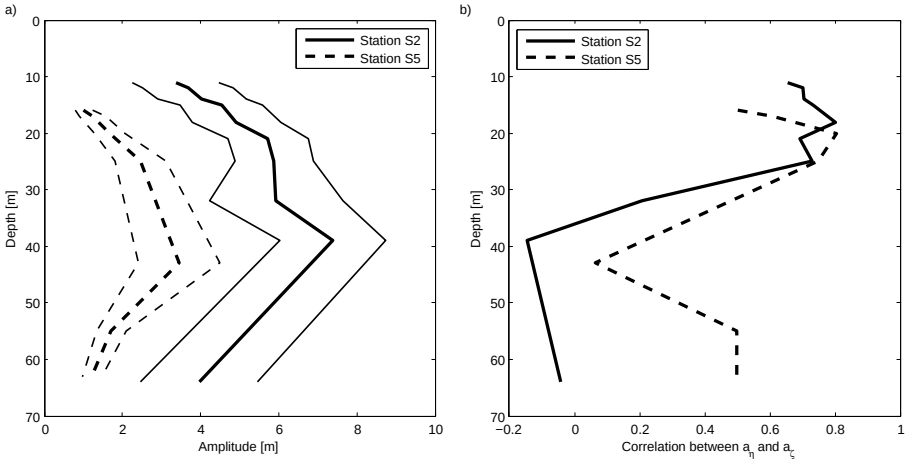

Fig. 7. **(a)** Amplitude of density surfaces as a function of depth at station S2 (solid lines) and station S5 (dashed lines). The mean amplitude is plotted with thick lines and the mean amplitude ± one standard deviation with thin lines (left panel). **(b)** Correlation coefficient between the surface amplitude and the amplitude of different density surfaces as a function of depth for station S2 (solid line) and station S5 (dashed line) (right panel).

OSD
9, 315–357, 2012

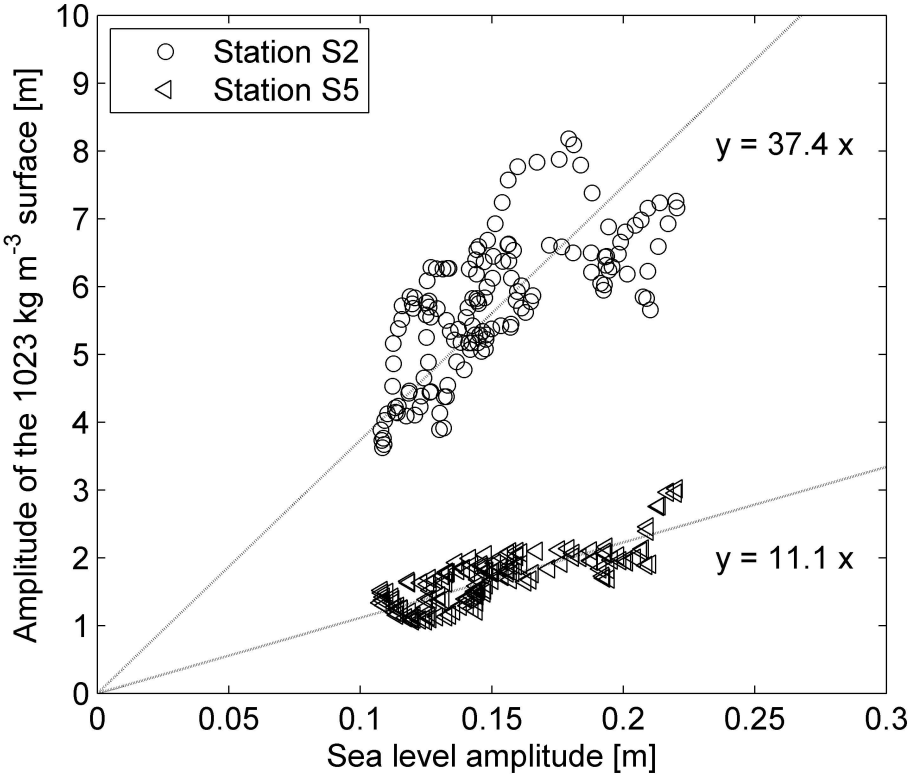

Fig. 8. The amplitude of the 1023 kg m^{-3} density surface at station S2 (circles) and S5 (triangles) plotted as a function of the sea level amplitude. The dashed lines are least square fits intercepting the origin.

OSD
9, 315–357, 2012

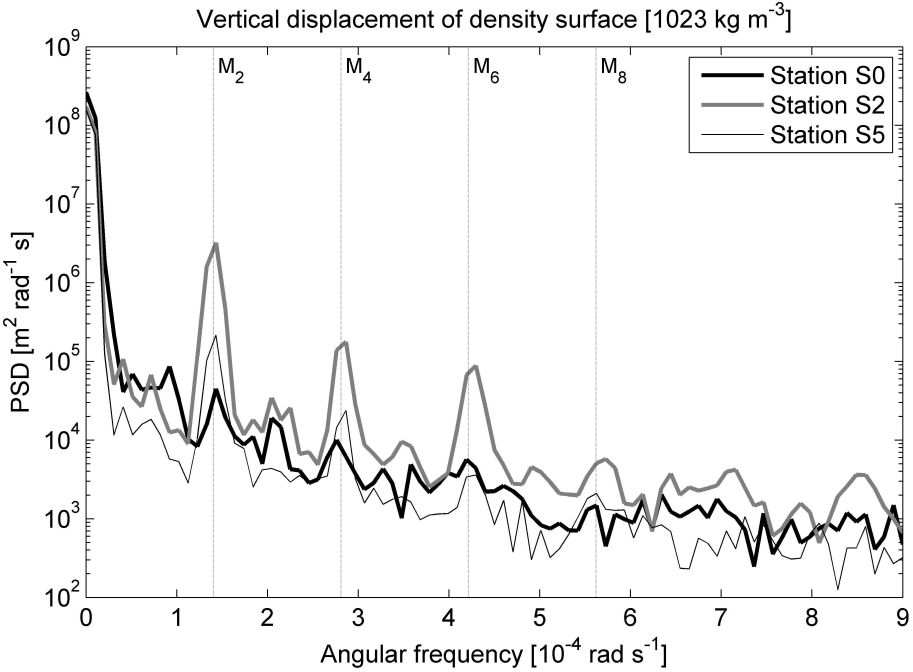

Fig. 9. Power spectral density (PSD) for the 1023 kg m^{-3} density surface at station S0, S2 and S5 as a function of the angular frequency.

OSD
9, 315–357, 2012

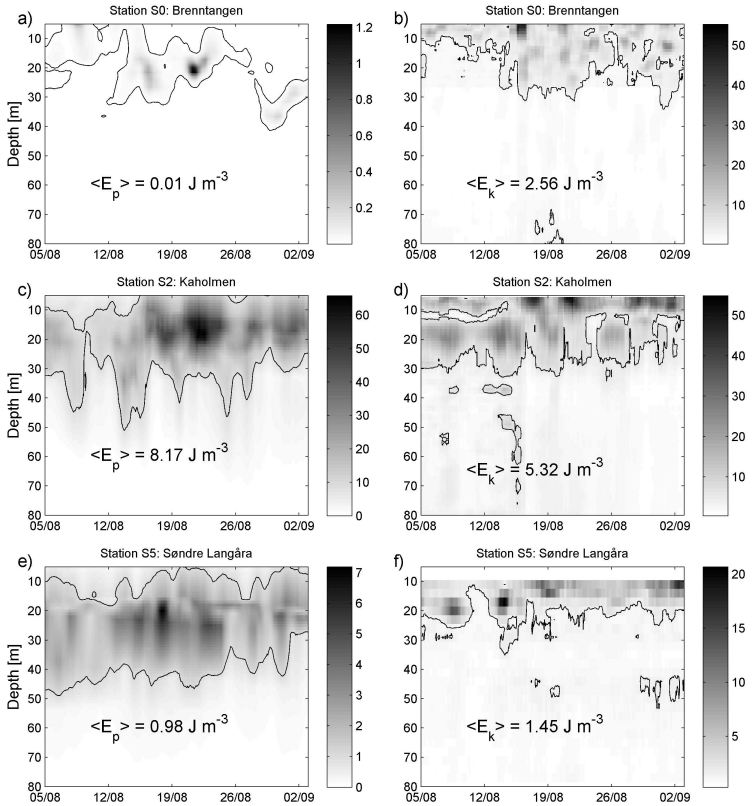

Fig. 10. Perturbation energy densities are shown with a grey scale where darker shades indicate higher values in unit J m^{-3} for stations S0 (**a** and **b**), S2 (**c** and **d**) and S5 (**e** and **f**). Potential energy density E_p Eq. (8) is shown to the left and kinetic energy density E_k Eq. (9) to the right. The average of the energy densities $\langle E_p \rangle$ and $\langle E_k \rangle$ for the whole period and for all depths is indicated with a number, and a contour line with this value is drawn in each plot.

OSD
9, 315–357, 2012

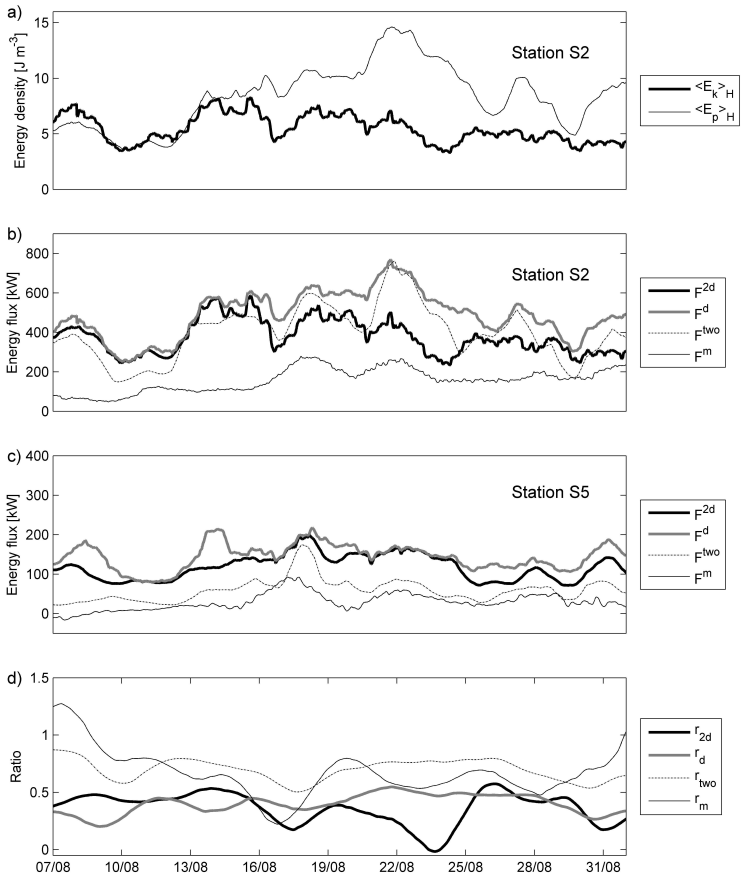

Fig. 11. **(a)** The depth-averaged perturbation energy densities $\langle E_p \rangle$ and $\langle E_k \rangle$ at station S2. **(b–c)** The energy flux F calculated with different methods at stations S2 and S5. **(d)** The ratio r of the energy flux that dissipates in Basin 1 calculated from Eq. (19).

OSD
9, 315–357, 2012

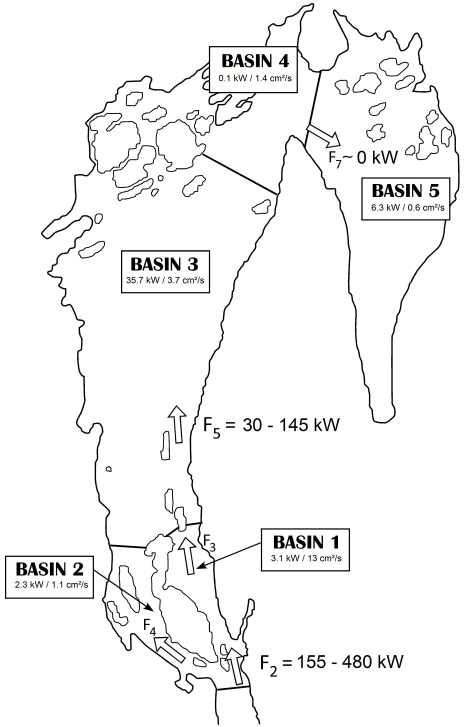

Fig. 12. Fluxes F of internal wave energy entering and leaving the different basins (highest and lowest values from Table 2) are shown in a schematic map of the inner Oslofjord. The results from calculations at stations S2 and S5 are indicated with the highest and lowest result next to the arrows. The integrated work against buoyancy calculated from Eq. (20) with unit kW and the depth averaged diffusivity coefficient Eq. (21) with unit $cm^2\,s^{-1}$ below 20 m depth are indicated for each basin.

OSD
9, 315–357, 2012